

Alignment of Magnetized Accretion Disks and Relativistic Jets with Spinning Black Holes

Jonathan C. McKinney,^{12*} Alexander Tchekhovskoy,³ Roger D. Blandford¹

¹Kavli Institute for Particle Astrophysics and Cosmology, Stanford University,
PO Box 20450, MS 29, Stanford, CA 94309, USA

²University of Maryland at College Park, Dept. of Physics, Joint Space-Science Institute
1117 John S. Toll Building #082, College Park, MD 20742, USA

³Center for Theoretical Science, Jadwin Hall, Princeton University, Princeton,
NJ 08544 USA; Princeton Center for Theoretical Science Fellow

*To whom correspondence should be addressed; E-mail: jcm@umd.edu .

Accreting black holes (BHs) produce intense radiation and powerful relativistic jets, which are affected by the BH's spin magnitude and direction. While thin disks might align with the BH spin axis via the Bardeen-Petterson effect, this does not apply to jet systems with thick disks. We used fully three-dimensional general relativistic magnetohydrodynamical simulations to study accreting BHs with various BH spin vectors and disk thicknesses with magnetic flux reaching saturation. Our simulations reveal a “magneto-spin alignment” mechanism that causes magnetized disks and jets to align with the BH spin near BHs and further away to reorient with the outer disk. This mechanism has implications for the evolution of BH mass and spin, BH feedback on host galaxies, and resolved BH images for SgrA* and M87.

Astrophysical black holes (BHs) operate as engines that convert gravitational binding energy

of accreting plasmas into intense radiation (1) and release BH spin energy (2–4) into powerful relativistic jets (5, 6). Relativistic jets from accreting BHs are commonly observed to emerge from active galactic nuclei (AGN) or quasars, x-ray binaries as microquasars, and gamma-ray burst (GRB) events. GRB jets allow one to probe the earliest epochs of star formation, whereas radiation and jets from AGN play a direct dynamical role via feedback that suppresses star formation in their host galaxies (7).

BHs are also intrinsically interesting because they act as laboratories for probing Einstein’s general relativity theory and for testing theories about accreting BHs and jets. Astrophysical BHs are characterized primarily by their mass (M) and dimensionless spin angular momentum (j). BHs have been measured to have masses of tens to billions of solar masses, like M87’s BH with $M \sim 6 \times 10^9 M_\odot$ (8). Spins have also been measured and span the whole range of possible values, including near the maximal value of $j \sim 1$ in the BH x-ray binary GRS1915+105 with $M \sim 14 M_\odot$ and in the AGN MCG-6-30-15 with $M \sim 3 \times 10^6 M_\odot$ (9, 10). Structures on BH event horizon length scales have recently been resolved by Earth-sized radio telescope interferometry for SgrA* (11, 12) and M87 (13, 14).

The BH spin/rotational axis generally points in a direction that is tilted by some angle θ_{tilt} relative to the rotational axis of the plasma disk and its magnetic field’s direction at large distances. While the BH’s present angular momentum axis is set by the history of plasma accretion and mergers with other BHs, the gas being currently supplied (at mass accretion rate \dot{M}) to the BH can have an arbitrarily different angular momentum axis. This tilt influences the intensity of the radiation via changes in the gravitational potential felt by the plasma and also influences what an observer at different viewing angles sees due to disk warping and jet bending.

One mechanism known to possibly affect the orientation of a disk or jet is the “Bardeen-Petterson” (BP) effect (15–18), where Lense-Thirring (LT) forces induced by the BH frame-dragging cause a misaligned disk to precess and warp until a local viscosity aligns a very thin

disk out to some distance (estimated to be out to $r \sim 10r_g - 10^5 r_g$, r_g is a gravitational radius (19), depending upon assumptions) from the BH. Whereas the viscosity has been thought to result from turbulence driven by the magneto-rotational instability (MRI) that amplifies weak small-scale ($\lesssim H$, the disk height) magnetic fields (20), magnetohydrodynamical (MHD) simulations of weakly magnetized disks have not yet seen any BP alignment effect (21). The BP effect and LT precession remain commonly invoked mechanisms to understand the way tilt affects how BH mass and spin evolve (22, 23), how merging BHs are affected by any nearby plasma (24), and how disks and their jets are oriented (25, 26).

Large-scale electromagnetic (EM) fields might also affect the jet's and disk's orientation via external confinement forces (27, 28). Estimates based upon large-scale magnetic fields being weaker than turbulent disk fields suggested that EM forces are insufficient to align the disk with the BH (27) or the BH with the disk (29, 30). Simulations without disks have given ambiguous results for the EM jet direction. For a uniform vertical magnetic field and no disk, the jet is directed along the magnetic field direction rather than the BH's tilted spin axis (31), whereas isolated magnetic threads tend to align with the BH spin axis when there is no disk to restrict their motion (32).

We have used fully three-dimensional (3D) general relativistic (GR) MHD simulations (33) of accreting BHs to show that near the BH both the disk and jet reorient and align with the BH's spin axis. Our simulations were designed so that the magnetic field built-up to a natural saturation strength with, roughly, the disk's thermal+ram+gravitational forces balancing the disk's and jet's magnetic forces such that the trapped large-scale magnetic field threading the BH and disk became strong compared to the disk's turbulent field. The saturated field strength has been demonstrated to be independent of the strength of the initial magnetic field when the surrounding medium has a sufficient supply of magnetic flux, weakly dependent upon BH spin, and proportionally dependent upon disk thickness (4, 28, 34). We considered various BH

spins (35), BH tilts, and disks with a quasi-steady state height H to radius R ratio of $H/R \sim 0.6$ for thick disks and $H/R \sim 0.3$ for thinner disks. Numerical convergence of our results was determined based upon both convergence quality measures for how well the MRI and turbulence was resolved (Table S2) and based upon explicit convergence testing (33).

Let us motivate these MHD simulations by estimating whether EM forces are expected to dominate LT forces on the rotating heavy disk. Imagine a toy model with a flat heavy disk tilted and pushed-up against the magnetized jet generated directly by the rotating BH. The EM torque per unit area by the jet on the disk is $\tau_{\text{EM}} \sim r B_r B_\phi / 4 \sim r^2 B_r^2 \Omega_F / 4$ for magnetic field B bending on scale r with field line rotation frequency $\Omega_F \sim j/8$ for $j \sim 1$ (28). Introducing a dimensionless magnetic flux of $\Upsilon \approx 0.7(4\pi r^2 B_r) / \sqrt{4\pi r_g^2 \dot{M} c}$ with B in Gaussian units (r_g and c reintroduced for dimensional clarity) that is consistent with measurements in our previous works (28), then $\tau_{\text{EM}} \sim \Upsilon^2 \dot{M} \Omega_F / (8\pi r^2)$. Meanwhile, the LT torque per unit area is $\tau_{\text{LT}} \sim \Omega_{\text{LT}} L$ with LT precession rate $\Omega_{\text{LT}} \sim 2j/r^3$, disk angular momentum per unit area $L \sim \Sigma r v_\phi$, disk surface density $\Sigma \sim \dot{M} / (2\pi r v_r)$, and far from the horizon an effective viscosity $\alpha_{\text{eff}} \sim v_r / ((H/R)^2 v_\phi)$. This gives $\tau_{\text{LT}} \sim j \dot{M} v_\phi / (\pi r^3 v_r)$. The ratio of the EM to LT torques for $j \sim 1$ is then $\tau_{\text{EM}} / \tau_{\text{LT}} \sim \Upsilon^2 r v_r / (64 r_g v_\phi)$, with r_g reintroduced for dimensional clarity. Far beyond the horizon,

$$\frac{\tau_{\text{EM}}}{\tau_{\text{LT}}} \sim \frac{1}{64} \Upsilon^2 \frac{r \alpha_{\text{eff}}}{r_g} (H/R)^2. \quad (1)$$

Over the horizon and in the jet, $\Upsilon \sim 10$ for our thinner disk models and $\Upsilon \sim 17$ for our thick disk models (28). Also, for both thicknesses, $(r/r_g) \alpha_{\text{eff}} \sim 15$ and roughly constant with radius while $v_r/v_\phi \sim 1$ near the horizon (28). So, at all distances, the jet's EM forces lead to $\tau_{\text{EM}}/\tau_{\text{LT}} \sim 2$ for our thinner disk models and $\tau_{\text{EM}}/\tau_{\text{LT}} \gtrsim 5$ for thick disk models. So, we expect EM forces to dominate LT forces for both our thinner and thick disk models (including for small spins (33)).

EM alignment forces are effective when they are larger than forces associated with the newly accreted rotating plasma with torque per unit area of $\tau_{\text{acc}} \sim \dot{M} v_\phi / (2\pi r)$. So, $\tau_{\text{EM}}/\tau_{\text{acc}} \sim$

$\Upsilon^2 \Omega_F / (4rv_\phi)$, and when these torques are equal one obtains an implicit equation for a “magneto-spin alignment” radius of

$$r_{\text{msa}} \sim \frac{\Omega_F r_g^2 \Upsilon^2}{4v_\phi}, \quad (2)$$

(with r_g reintroduced), within which EM forces can torque the accreting dense material. For sufficiently small Υ or j , no alignment can occur. We obtain $r_{\text{msa}} \gtrsim 30r_g$ for our thinner and thick disk models that are sub-Keplerian by a factor 0.5 to 0.1, respectively (28), although accurate estimates require more physics (33) or simulations.

Our self-consistent fully 3D GRMHD simulations started with a disk around an untilted BH where the BH spin axis, disk rotational axis, and emergent jet’s direction all pointed in the vertical (z) direction. As the simulation proceeded, the mass and magnetic flux readily advected from large distances onto the BH. The magnetic flux vs. radius saturated on the BH and within the disk near the BH once magnetic forces balanced the disk’s thermal+ram+gravitational forces. Magnetic braking causes such disks to become even more sub-Keplerian than weakly magnetized thick disks (28), which means the classical thin disk inner-most stable circular orbit position is even less applicable than for weakly magnetized thick disks. The simulations were evolved for a long time period so that the disk reached a quasi-stationary magnetically saturated state out to about $r \sim 40r_g$ (28, 33).

Then, the BH spin axis was instantly tilted by an angle of $\theta_{\text{tilt},0}$ (see Table 1 for tilts used for different spins and disk thicknesses). The tilted disk-jet system underwent a violent rearrangement for the larger tilts. The frame-dragging forces caused the nearly split-monopole BH magnetosphere to align with the BH spin axis, as expected because the misaligned angular momentum was radiated away as part of the electromagnetic outflow on Alfvén time scales. Then, the magnetic torque caused the heavy disk to lose its misaligned component of angular momentum and so reorient with the BH’s rotating magnetosphere. The timescale for alignment seems to be roughly the Alfvén crossing time near the heavy disk and BH. This “magneto-spin align-

ment” occurs because the magnetic field built-up to a natural saturation strength on the horizon where $\Upsilon \sim 10$ (depending upon the thickness and tilt), which led to the BH magnetosphere’s forces dominating the disk dynamics and LT forces.

All simulations (including with zero tilt) were then further evolved in time until all the tilted simulations reached a new quasi-stationary state out to $r \sim 40r_g$. This ensured that any differences at later times in the disk and jet between tilted and untilted simulations were due to the BH tilt. This also ensured that each of the tilted and untilted simulations reached their own quasi-steady state values for the magnetic flux near the BH, magnetic flux in the disk, mass accretion rate, etc. We then measured the evolved relative tilt between the BH spin axis and the disk & jet at $r = 4r_g$ and $r = 30r_g$ (Table 1). For all our models, the disk & jet aligned with the BH spin axis near the BH, whereas the disk axis & jet direction deviated at larger distances. Such deviations are expected because the jet interacted with circulation with stronger mass inflows at larger distances (33). Despite the tilts and jet deviations, the BH’s efficiency (defined as the ratio of energy out to energy in) was roughly 100% for $j \gtrsim 0.9$ (Table S1), where more tilt led to reduced efficiency due to more spatially and temporally irregular mass inflow.

Our most extreme case of a tilted BH accretion disk and jet system is the $j = 0.99$ model with a full tilt of $\theta_{\text{ilt},0} = 1.5708 \approx 90^\circ$ and disk thickness $H/R \sim 0.3$. Even in this extremely tilted case, the evolved disk and jet near the BH aligned with the BH spin axis (Fig. 1, Fig. S1, Movie S1). The jet’s magnetic field winded around the persistent relativistic jet, and the magnetic field was well-ordered even for this highly tilted case. The jet was not symmetric around the jet axis, and instead there was a broad wing (with opening half-angle of about 25° by $r = 40r_g$) and a narrow wing (with opening half-angle of about 5° by $r = 40r_g$). At large distances from the BH, the jet drilled its way through the disk material and gradually got pushed away from the disk (Fig. 2 and Movie S2). The magnetic field winded around with a pitch angle of about 45° near the BH and had a smaller pitch angle at larger distances. By $r \sim 300r_g$, the

Table 1: Tilted Black Hole Disk-Jet Systems

ModelName	BH j	Disk H/R	Initial Tilt	DiskTilt $r=4r_g$	JetTilt $r=4r_g$	DiskTilt $r=30r_g$	JetTilt $r=30r_g$
A0.94BfN40	0.9375	0.6	0	0	0	0	0
A0.94BfN40T0.35	0.9375	0.6	0.35	0.0	0.0	0.2	0.2
A0.94BfN40T0.7	0.9375	0.6	0.70	0.0	0.0	0.4	0.3
A0.94BfN40T1.5708	0.9375	0.6	1.5708	0.0	0.1	0.5	0.7
A-0.9N100	-0.9	0.3	0	0	0	0	0
A-0.9N100T0.15	-0.9	0.3	0.15	0.1	0.1	0.1	0.2
A-0.9N100T0.3	-0.9	0.3	0.30	0.2	0.2	0.2	0.2
A-0.9N100T0.6	-0.9	0.3	0.60	0.2	0.3	0.4	0.3
A-0.9N100T1.5708	-0.9	0.3	1.5708	0.2	0.4	0.9	0.8
A0.9N100	0.9	0.3	0	0	0	0	0
A0.9N100T0.15	0.9	0.3	0.15	0.0	0.0	0.1	0.1
A0.9N100T0.3	0.9	0.3	0.30	0.1	0.1	0.2	0.2
A0.9N100T0.6	0.9	0.3	0.60	0.1	0.1	0.3	0.3
A0.9N100T1.5708	0.9	0.3	1.5708	0.2	0.3	0.7	0.6
A0.99N100	0.99	0.3	0	0	0	0	0
A0.99N100T0.15	0.99	0.3	0.15	0.0	0.1	0.1	0.1
A0.99N100T0.3	0.99	0.3	0.30	0.1	0.1	0.2	0.2
A0.99N100T0.6	0.99	0.3	0.60	0.1	0.1	0.3	0.4
A0.99N100T1.5708	0.99	0.3	1.5708	0.1	0.1	0.6	0.6

Table 1: The simulation models listed by model name, which identifies the approximate BH spin of $j = x$ (giving Ax), something about the magnetic field choices for some y and z (giving ByNz) (28), and the initial relative tilt ($\theta_{\text{tilt},0} = p$ in radians) between the BH spin axis and the disk rotation axis (giving Tp, where no T means $\theta_{\text{tilt},0} = 0$). The second column gives the dimensionless BH spin (j), the third column gives the evolved quasi-steady state value of the disk height-to-radius ratio H/R between $r \sim 20r_g$ and $r \sim 30r_g$, while the fourth column identifies the initial relative tilt ($\theta_{\text{tilt},0}$) between the disk+jet (having the same tilt initially) and the BH spin axis. The fifth and sixth columns give the evolved relative tilt between the BH spin axis and the disk & jet, respectively, at $r = 4r_g$. The seventh and eighth columns give the same measurements at $r = 30r_g$. A relative tilt of 0.0 means the disk or jet remained aligned with the BH spin axis, while a tilt equal to the initial tilt means the disk or jet was unaffected.

jet had become parallel with (but offset from) the outer disk rotational axis, and so the jet and counter-jet were also offset.

Thus, our simulations have revealed a “magneto-spin alignment” mechanism that aligns the disk & jet axes with the BH spin axis near the BH once the magnetic field has saturated on the BH and within the disk (36). Unlike the BP effect, the mechanism actually works best for thick disks, and so the magneto-spin alignment mechanism should control jet systems where thick disks (due to accretion at either very low (37) or very high rates when $H/R \gtrsim 0.5$) are expected. For example, for SgrA* and M87, if the BHs rotate sufficiently rapidly (33), then we expect their jet’s and disk’s photon spectra, temporal behaviors, and resolved images to be affected by non-zero relative tilts due to disk warping and jet bending near the BH.

Tidal disruption flare events like Swift J164449.3 +573451 are thought to be produced by very high accretion rates onto BHs, which launch fairly persistent jets that dissipate and give the observed emission (38). Our results suggest the inner disk and inner jet are both aligned with the BH spin axis, but the observed jet dissipating at large distances need not point along the BH spin axis. EM forces do not directly cause any precession (27), so the lack of LT precession-induced variability does not alone imply that the jet is necessarily driven by the BH spin power (26). Further, quasi-periodic oscillations (39) and long-term dips seen in this system’s light curve might be explained by oscillations in the disk-jet magnetospheric interface (28) or by periods of magnetic flux accumulation and rejection by the BH (4) (both occurring for untilted systems) rather than by LT precession.

Jet dissipation/emission (e.g. in blazars) might be due to the jet ramming into the disk until the jet aligns with the disk rotational axis at large distances. Measurements of BH spin in AGN and x-ray binaries might be affected by assumptions about the alignment between the disk, BH spin, and jet (9, 10). The cosmological evolution of BH mass and spin and AGN feedback for accretion at high rates might be affected by the higher BH spin-down rates and jet efficiencies

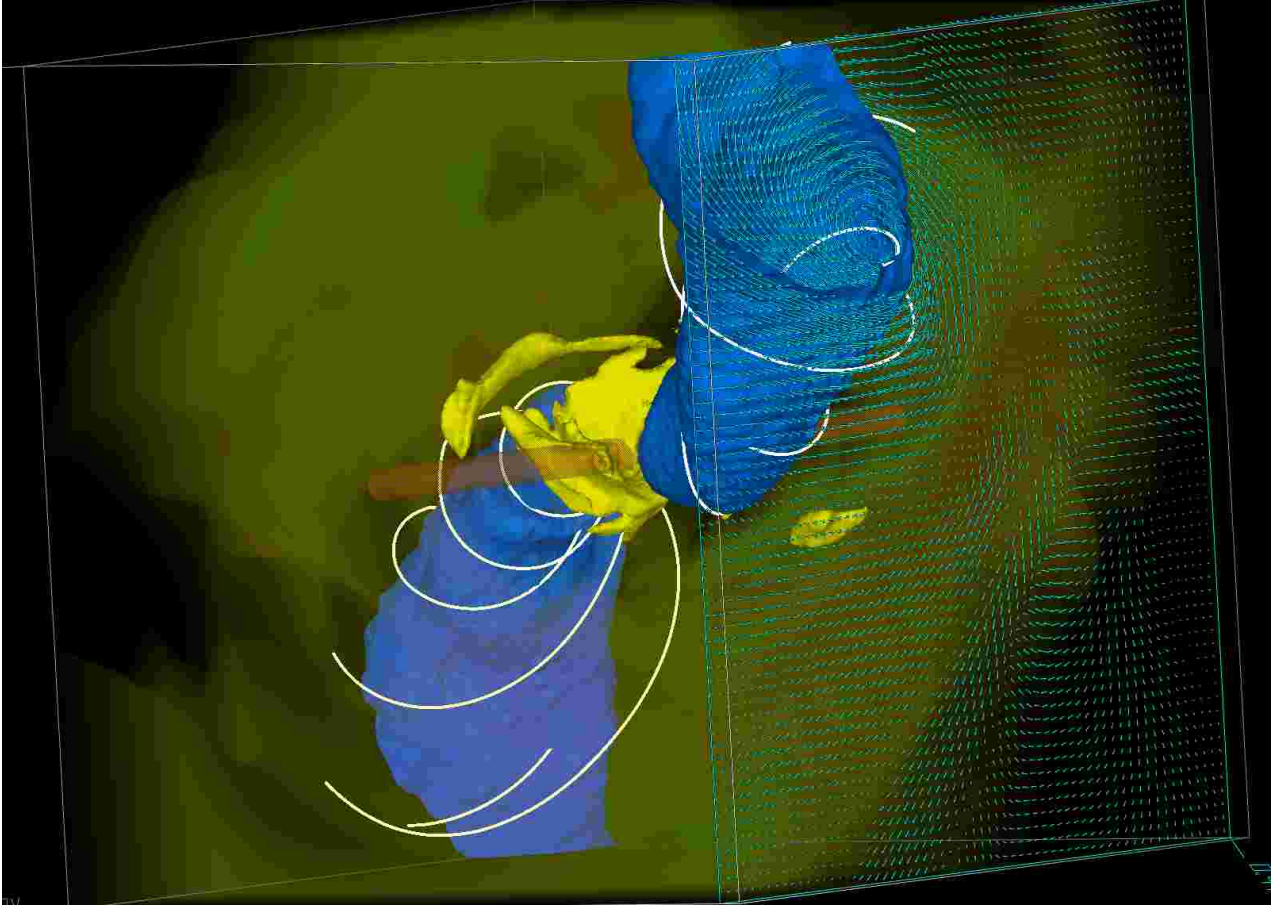


Figure 1: 3D snapshot for an evolved model with $j = 0.99$, initial relative tilt $\theta_{\text{tilt},0} \approx 90^\circ$, and disk thickness of $H/R \sim 0.3$. The rotating BH sits at the center of the box of size $r = -40r_g$ to $r = +40r_g$ in each dimension. The snapshot shows the disk near the BH (yellow isosurface, which is mostly flat in the figure plane), the highly magnetized jet region (blue isosurface, with magnetic energy per unit rest-mass energy equal to about 70), the rotational axis of the disk both initially and at large distances (orange cylinder), outer disk (green-yellow volume rendering, more aligned with disk rotational axis at large distances), magnetic field vectors (like iron filings on that surface) for a cross-section of the jet (cyan vectors), and jet magnetic field lines (white lines) that trace from the BH out to large distances. The disk and jet near the BH are aligned with the BH spin axis and point mostly in-out of the figure plane, while at larger distances the jet points roughly half-way between the BH spin axis and the disk's rotational axis at large distances (pointing along the orange cylinder).

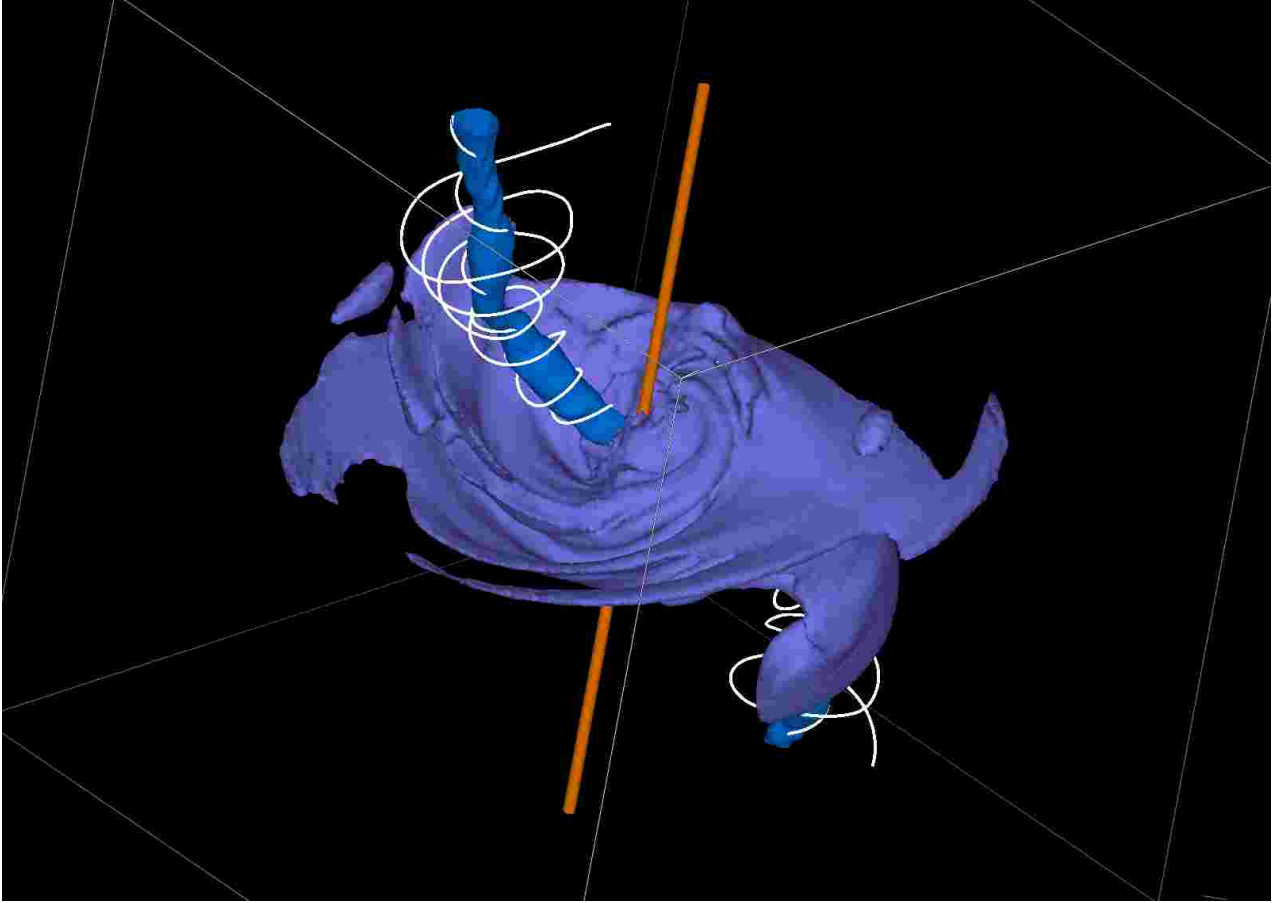


Figure 2: 3D snapshot that is similar to Fig. 1 but shows the outer disk (density isosurface in purple) at large distances from the BH in a box of size $r = -350r_g$ to $r = 350r_g$ in each dimension. The jet (blue isosurface, here with magnetic energy per unit rest-mass energy equal to about 4, still corresponding to the jet spine) is aligned with the BH spin near the BH but gradually gets pushed by the disk material and becomes parallel to (but offset from) the disk rotational axis at large distances. The strong interaction between the jet and disk has left an asymmetry or warp in the disk density at large radii.

compared to standard thin disk spin-down rates and radiative efficiencies (28) and also by how the jet aligns the disk material before LT torques can be effective so possibly leading to less change in the BH spin direction compared to the BP effect.

References and Notes

1. N. I. Shakura, R. A. Sunyaev, *A&A* **24**, 337 (1973).
2. R. D. Blandford, R. L. Znajek, *MNRAS* **179**, 433 (1977).
3. S. Koide, K. Shibata, T. Kudoh, D. L. Meier, *Science* **295**, 1688 (2002).
4. A. Tchekhovskoy, R. Narayan, J. C. McKinney, *MNRAS* **418**, L79 (2011).
5. R. V. E. Lovelace, *Nature* **262**, 649 (1976).
6. M. C. Begelman, M. J. Rees, R. D. Blandford, *Nature* **279**, 770 (1979).
7. T. Di Matteo, V. Springel, L. Hernquist, *Nature* **433**, 604 (2005).
8. K. Gebhardt, *et al.*, *ApJ* **729**, 119 (2011).
9. C. S. Reynolds, A. C. Fabian, *ApJ* **675**, 1048 (2008).
10. J. E. McClintock, *et al.*, *arXiv/0911.5408* (2009).
11. S. S. Doeleman, *et al.*, *Nature* **455**, 78 (2008).
12. V. L. Fish, *et al.*, *ApJ* **727**, L36 (2011).
13. K. Hada, *et al.*, *Nature* **477**, 185 (2011).
14. S. S. Doeleman, *et al.*, *Science* **338**, 355 (2012).

15. J. M. Bardeen, J. A. Petterson, *ApJ* **195**, L65 (1975).
16. S. P. Hatchett, M. C. Begelman, C. L. Sarazin, *ApJ* **247**, 677 (1981).
17. S. Kumar, J. E. Pringle, *MNRAS* **213**, 435 (1985).
18. R. P. Nelson, J. C. B. Papaloizou, *MNRAS* **315**, 570 (2000).
19. We typically set $GM = c = 1$, where c is the speed of light, G is the gravitational constant, and M is the mass of the BH, so that $r_g \equiv GM/c^2 = 1$. For dimensional clarity, these constants are sometimes reintroduced.
20. S. A. Balbus, J. F. Hawley, *ApJ* **376**, 214 (1991).
21. P. C. Fragile, O. M. Blaes, P. Anninos, J. D. Salmonson, *ApJ* **668**, 417 (2007).
22. M. C. Begelman, R. D. Blandford, M. J. Rees, *Nature* **287**, 307 (1980).
23. A. Perego, M. Dotti, M. Colpi, M. Volonteri, *MNRAS* **399**, 2249 (2009).
24. T. Bogdanović, C. S. Reynolds, M. C. Miller, *ApJ* **661**, L147 (2007).
25. P. Natarajan, P. J. Armitage, *MNRAS* **309**, 961 (1999).
26. N. Stone, A. Loeb, *Physical Review Letters* **108**, 061302 (2012).
27. A. R. King, J. P. Lasota, *A&A* **58**, 175 (1977).
28. J. C. McKinney, A. Tchekhovskoy, R. D. Blandford, *MNRAS* **423**, 3083 (2012).
29. H. Kim, H. K. Lee, C. H. Lee, *JCAP* **9**, 1 (2003).
30. A. R. King, *Magnetic Fields in the Universe: From Laboratory and Stars to Primordial Structures.*, E. M. de Gouveia dal Pino, G. Lugones, A. Lazarian, eds. (2005), vol. 784 of *American Institute of Physics Conference Series*, pp. 175–182.

31. C. Palenzuela, T. Garrett, L. Lehner, S. L. Liebling, *Phys. Rev. D* **82**, 044045 (2010).
32. V. Semenov, S. Dyadechkin, B. Punsly, *Science* **305**, 978 (2004).
33. Materials and Methods are available as supplementary materials on *Science* Online.
34. A. Tchekhovskoy, J. C. McKinney, *MNRAS* **423**, L55 (2012).
35. Spins of $j \sim 0.9$ give mid-range BH rotation rates. See the Physical Models section in the supplement.
36. The magnetic field built-up via direct magnetic flux advection, but the build-up might also occur via dynamo generation as seen in our prior untilted simulations that showed emergent large-scale dipolar flux patches.
37. R. Narayan, I. Yi, R. Mahadevan, *Nature* **374**, 623 (1995).
38. J. S. Bloom, *et al.*, *Science* **333**, 203 (2011).
39. R. C. Reis, *et al.*, *Science* **337**, 949 (2012).

Acknowledgements:

JCM thanks Narayan, Dexter, and Fragile for useful discussions, and Ralf Kaehler at KIPAC (SLAC/Stanford) for the artistic rendering in Figure S1. This work was supported by a NASA Fermi grant NNX11AO21G (JCM), Princeton Center for Theoretical Science Fellowship (AT) and NSF/XSEDE resources provided by TACC (Lonestar/Ranch) and NICS (Kraken) under the awards TG-PHY120005 (JCM) and TG-AST100040 (AT) and provided by NASA (NAS Pleiades) for the Fermi grant. GRMHD simulation data are contained in Table 1 and Tables S1 to S2 in the Supporting Online Materials.

Supplementary Materials:

www.sciencemag.org

Materials and Methods

Fig. S1

Tables S1 S2

Movies S1 S2

References (40-98)



Supplementary Materials for

Alignment of Magnetized Accretion Disks and Relativistic Jets with Spinning Black Holes

Jonathan C. McKinney*, Alexander Tchekhovskoy, Roger D. Blandford

*To whom correspondence should be addressed; E-mail: jcm@umd.edu .

This PDF file includes:

Materials and Methods

Fig. S1

Tables S1 to S2

Captions for Movies S1 to S2

References (40-98)

Other Supplementary Materials for this manuscript includes the following:

Movies S1 to S2

1 Methods

In this supporting text, we describe our numerical methods, elaborate on details for the toy model in the report that estimates the effects of magnetic fields vs. Lense-Thirring precession around tilted black holes (BHs), present the equations of motion we numerically solve, discuss the diagnostics computed, and summarize the setup of our physical and numerical models.

1.1 Numerical Methods

We used fully three-dimensional (3D) general relativistic magnetohydrodynamic (GRMHD) simulations to study BH accretion flows with various BH spins (dimensionless value of j), relative tilts between the BH spin axis and the angular momentum (rotational) axis at large radii ($\theta_{\text{tilt},0}$ in radians), and both thick and thinner disks (height H to radius R ratio of $H/R \sim 0.6$ and $H/R \sim 0.3$, respectively).

Our simulations used the GRMHD code HARM based upon a conservative shock-capturing Godunov scheme with 2nd order Runge-Kutta time-stepping, Courant factor 0.8, Lax Friedrichs (LAXF) fluxes, simplified wave speeds, piecewise parabolic method (PPM) type interpolation (with no contact steepener, but with shock flattener based upon rest-mass flux density and total pressure), a staggered magnetic field representation, and a regular grid warping (40–42) as used in our prior works(28). A free version of HARM is available online for download (43). The HARM code has several key features that make it suitable for highly magnetized regions around BHs with tilted orientations (see appendix of (28)). In particular, the spherical polar coordinate axis is treated using transmissive (not reflective) boundary conditions so that the dissipation near the axis is kept to a minimum. This transmissive boundary condition treats all quantities in boundary cells near the axis as smooth and continuous functions whose values coincide with the non-boundary cells on the other side of the axis. This allows the flow and any components of the magnetic field to pass directly through the polar axis with little artificial dissipation while

maintaining a robust solution via the Godunov scheme.

1.2 Toy Model

In this section, we give more details about the toy model introduced in the report.

The nature of jets around BHs has been a topic of interest for a long time (44–50). Our focus is on how the disk and jet are affected by a relative tilt with respect to the BH spin axis. Tilted BHs have been studied at an idealized level for a few decades. Solutions have been found for static scalar and vacuum magnetic fields around rotating BHs with relative tilt (51–55). For a vacuum magnetic field, it was found that the BH would be penetrated by non-zero magnetic flux for a maximally spinning ($j = 1$) BH only if there were relative tilt (54). Torque on a charged BH was also considered (56). For a review of these idealized works, see (55). Simulations have been required in order to push beyond these early idealized models, with some advances for simulations without tilt (for a review, see (57, 58)). Some axisymmetric simulations without tilt also see flow reversal near the BH (59), with the effect being quite strong once the magnetic field strength saturates (28). Untilted simulations have so far only studied how strong magnetic fields affect the aligned component of the BH spin (60) and (28). So far, no GRMHD simulations with tilt show any Bardeen-Petterson type alignment effect (21). Modern simulations of relatively thin weakly magnetized disks tilted relative to the BH spin axis have been studied, including the effect of tilt on the inner-most stable circular orbit (ISCO) (61), the development of shocks in the disk near the BH (62), the effect of tilt on observations of BH accretion disks (63, 64), and the effect on neutron star-BH mergers (65). Simulations of tilted disks with naturally saturated magnetic field strengths are required to understand how disks and jets are oriented under generic circumstances. Astrophysical applications justifiably only so-far invoke the Bardeen-Petterson effect as a possible alignment effect (48, 66–81), because no other type of alignment effect has yet been demonstrated in any GRMHD simulations and all theoretical arguments suggested that

magnetic torque alignment would not occur (27).

Here we estimate the ratio of the electromagnetic (EM) force on the heavy disk relative to the Lense-Thirring (LT) force on the rotating heavy disk. This argument was used to get roughly correct the factors of order unity that appear in the report. We also account for some other subtle effects, like disk thinning, not accounted for in the report. Imagine a toy picture with a flat heavy disk tilted with respect to a rotating BH, with both the BH and disk threaded by a magnetic field (\mathbf{B}) that bends on scale of radius r . The magnetic field is nearly co-rotating with the BH-disk system, which drives a current (\mathbf{J}) into the ambient medium. Then, the EM torque per unit area on the disk by magnetic stresses is $\tau_{\text{EM}} \equiv L_{\text{EM}}/dt \sim |\int d\theta \sin \theta \mathbf{r} \times (\mathbf{J} \times \mathbf{B})| \sim \pi \sin \theta_{\text{tilt}} r B_r B_\phi / (4\pi)$ for radial field B_r , toroidal field $B_\phi \sim r \sin \theta \Omega_F B_r$ for field line angular frequency of rotation of Ω_F , and absolute magnetic flux on a radial shell of $\Phi \sim 4\pi r^2 |B_r|$ with dimensionless magnetic flux of $\Upsilon \approx 0.7\Phi / \sqrt{4\pi r_g^2 \dot{M} c}$ for Φ in Gaussian units (28). We focus on the jet with a roughly constant magnetic flux Φ , while the magnetic field threading the disk would enhance the EM forces. The LT torque per unit area is $\tau_{\text{LT}} \equiv dL_{\text{LT}}/dt \sim |\mathbf{\Omega}_{\text{LT}} \times \mathbf{L}| \sim \sin \theta_{\text{tilt}} \Omega_{\text{LT}} L$ with $|\mathbf{\Omega}_{\text{LT}}| = 2|\mathbf{J}_{\text{BH}}|/r^3 = 2j/r^3$ for disk angular momentum per unit area $L \sim \Sigma r v_\phi$, disk surface density $\Sigma \sim \dot{M}/(2\pi r v_r)$, effective viscosity $\alpha_{\text{eff}} \sim v_r/(G(H/R)^2 v_\phi)$, and $G \sim 1$ accounts for GR corrections (28). Even untilted disks that reach magnetic flux saturation undergo magnetic braking that (in addition to the disk being thick) leads to $\alpha_{\text{eff}} \sim 1$ and quite sub-Keplerian rotation (28), which makes us expect a) smaller LT forces ; b) EM forces can more easily change the disk rotational axis ; and c) the classical ISCO position is even less applicable than for weakly magnetized thick disks. The ratio of the EM to LT torques is then $\tau_{\text{EM}}/\tau_{\text{LT}} \sim \Upsilon^2 (r_g \Omega_F)/(c j) (r v_r)/(8 r_g v_\phi)$, with c and r_g reintroduced for clarity. Far from the horizon, one can write this ratio as

$$\frac{\tau_{\text{EM}}}{\tau_{\text{LT}}} \sim \frac{1}{8} \Upsilon^2 \left(\frac{r_g \Omega_F}{c j} \right) \frac{r \alpha_{\text{eff}}}{r_g} G(H/R)^2. \quad (1)$$

Assume the free parameters are $j \sim 1$, $\dot{M}(r)$ constant as valid for $r \lesssim 30 r_g$, $\Omega_F \sim \Omega_H/4 =$

$j/(8(1 + \sqrt{1 - j^2})) \sim j/8$ for the jet magnetosphere near the disk, and $\Upsilon \sim 10\text{--}17$ for our thinner and thick models, respectively (28). Also, over $r \sim 12r_g\text{--}20r_g$, the radially averaged $\alpha_{\text{eff}} \sim 1\text{--}0.4$ (with $(r/r_g)\alpha_{\text{eff}}$ roughly constant over the solution) and $H/R \sim 0.3\text{--}0.4$, respectively for the thinner and thick models, where the thicker disk undergoes some compression by magnetic forces (28). For our thinner models we get $\tau_{\text{EM}}/\tau_{\text{LT}} \sim 2$ while our thicker models get $\tau_{\text{EM}}/\tau_{\text{LT}} \sim 4$. So, we expect EM forces to dominate LT forces for roughly $H/R \gtrsim 0.2$ at $r \sim 10r_g\text{--}20r_g$. In addition, near the horizon, $v_r/v_\phi \sim 1$ (28), so near the horizon one obtains $\tau_{\text{EM}}/\tau_{\text{LT}} \sim 2$ for thinner models and $\tau_{\text{EM}}/\tau_{\text{LT}} \sim 5$ for thicker models. For non-zero spin, the value of Υ is roughly constant as a function of spin for both the thinner and thick disk models (28), so these estimates suggest EM torques dominate LT torques for all spins.

The additional EM force by frame-dragging on the magnetic field threading the disk gives $\Upsilon \propto r$ in the disk (34) and naively $\Omega_{\text{F}} \propto r^{-3}$, which apparently leads to LT forces eventually dominating over the disk's internal EM forces at large radii (but the jet's EM forces external to the disk can still dominate LT forces as discussed above). However, significant BH spin energy and angular momentum is fed directly into the disk itself (28), which leads to angular momentum transport that forces the disk's magnetic field to rotate a bit closer to the BH magnetosphere's value of Ω_{F} even far from the BH (e.g. the rotation of the fluid flow completely re-aligns with the BH spin direction out to $r \sim 40r_g$ for untilted retrograde ($j = -0.9375$) thick disks ($H/R \sim 0.6$) such that the flow is no longer retrograde and has the same radial profile of v_ϕ but simply with an opposite sign compared to the otherwise identical model with $j = +0.9375$ (28)).

Using a similar analysis as above we can *roughly* estimate whether the jet's EM forces actually affect the flow. Such an analysis is easier than for the BP effect that requires a model of the assumed local viscosity that would be due to MHD turbulence, while large-scale EM fields directly affect the plasma. The torque per unit area associated with the newly accreted rotating

plasma at some fixed Eulerian radius is $\tau_{\text{acc}} \sim \dot{M}v_\phi/(2\pi r)$ so that $\tau_{\text{EM}}/\tau_{\text{acc}} \sim \Upsilon^2\Omega_{\text{F}}/(4rv_\phi)$. This gives a “magneto-spin alignment” radius of

$$r_{\text{msa}} \sim \frac{\Omega_{\text{F}}r_g^2\Upsilon^2}{4v_\phi} \quad (2)$$

(with r_g reintroduced) where the torques are equal, within which EM forces can torque the accreting dense material. For our thinner disk models and $j \sim 1$ with $v_\phi \propto r^{-1/2}$ (but sub-Keplerian in magnitude by a factor of 0.5) (28), the jet’s external EM forces control the disk orientation out to $r \sim 40r_g$. For our thick disk models and $j \sim 1$ with $v_\phi \propto r^{-1}$ (or Keplerian with a reduction factor of 0.1) out to $r \sim 30r_g$ up to where a steady-state was reached (28), EM forces can easily torque the disk out to $r \sim 30r_g$ and may even dominate out to $r \sim 10000r_g$ if the flow remains the same factor below Keplerian at such large radii (as is possible for thick disks that reach magnetic field strength saturation out to large radii).

The magneto-spin alignment radius might depend upon spin. It is possible that for sufficiently slowly spinning BHs that produce weak jets, there might be no magneto-spin alignment effect. While rapidly rotating BHs might exist in SgrA* and M87 as some models/estimates show (82) and (14), this is still in debate (83, 84), so it is important to roughly estimate how spin might affect our results. For example, from Equation (2) and for the near-horizon region (i.e. $r \sim r_g$), horizon-scale alignment due to the jet alone occurs for $j \gtrsim 0.5$ for our thinner disk models and $j \gtrsim 0.2$ for our thick disk models if we use $v_\phi \sim 0.5c$ as valid for the near-horizon when $j \sim 1$ (e.g., see figure 7 in (28)). However, more generally, over a range of spins, $v_\phi \sim r_g\Omega_{\text{F}}$ near the horizon due to the BH dragging the magnetic field that then drags the plasma (4,34,28), so our estimates imply that all spins would allow for magneto-spin alignment of the disk close to the BH event horizon.

The magneto-spin alignment radius might also depend upon the existence of mass inflow-outflow circulation that is commonly seen in thick disk simulations. The BH jet value of Υ is

determined by force balance with the ingoing accretion near the horizon, but at larger radii one expects thick disks to produce winds that scale as $\dot{M}_{\text{wind}} \propto r$ and so have an ingoing accretion rate following $\dot{M}_{\text{in}} \propto r$ (28), such that the EM forces are eventually ineffective against the heavy mass inflow forces. Stated another way, the local Υ becomes too small in terms of the jet magnetic flux per unit square root of the local mass inflow rate. So, at some radius one expects the disk inflow to dominate the jet and for both the disk and jet to be parallel to the rotation axis of the outer disk (as consistent with the tilted simulations presented in this report).

These estimates suggest that if an astrophysical system were to have a truncated thick disk inside $r \sim r_{\text{msa}}$ and still reach magnetic field strength saturation, then the entire disk and jet would mostly align with BH spin.

These estimates also suggest that prior GRMHD simulations of tilted disks see no alignment effect (21) because their models have $H/R \sim 0.1\text{--}0.2$ and have a limited amount of magnetic flux available for accretion, both implying a small Υ so the EM jet cannot dominate the disk dynamics and EM forces cannot dominate LT forces. For example, the standard “thick” torus with $H/R \sim 0.2$ with a single poloidal field loop in the initial torus is used in many GRMHD simulations. This setup is similar to the one we studied a few years ago (85) that we recently realized leads to limited magnetic flux with $\Upsilon \sim 2$ near the BH and so leads to low jet efficiencies despite a spin of $j \sim 0.9$ (28). Using $\Upsilon \sim 2$ in our above analysis shows that magneto-spin alignment does not occur for any normal range of spins (i.e. $-1 \leq j \leq +1$), which is consistent with existing tilted MHD simulations (21).

Given the many non-trivial effects involved, simulations are optimal in order to obtain an accurate self-consistent solution once the magnetic field strength saturates so that all competing forces and effects can be accounted for.

1.3 Governing Equations

We solved the GRMHD equations for a magnetized accretion flow around a tilted rotating BH defined by the Kerr metric in Kerr-Schild coordinates with internal coordinates $\underline{x}^\alpha \equiv (t, \underline{x}^{(1)}, \underline{x}^{(2)}, \underline{x}^{(3)})$ mapped to the spherical polar coordinates $\underline{r}^\alpha \equiv (t, r, \theta, \phi)$. The z-axis of the spherical polar coordinate Kerr solution was rotated around the y-axis by $\theta_{\text{tilt},0}$ (86). We write orthonormal vectors as u_i , contravariant (covariant) vectors as \underline{u}^i (\underline{u}_i), and higher-ranked coordinate basis tensors with no underbar. We work with Heaviside-Lorentz units, often set $c = GM = 1$, and let the horizon radius be r_H .

Mass conservation gives

$$\nabla_\mu(\rho_0 \underline{u}^\mu) = 0, \quad (3)$$

where ρ_0 is the rest-mass density, \underline{u}^μ is the contravariant 4-velocity, and $\rho = \rho_0 \underline{u}^t$ is the lab-frame mass density.

Energy-momentum conservation gives

$$\nabla_\mu T^\mu_\nu = 0, \quad (4)$$

where the stress energy tensor T^μ_ν includes both matter (MA) and electromagnetic (EM) terms:

$$\begin{aligned} T^{\text{MA}\mu}_\nu &= (\rho_0 + e_g + p_g) \underline{u}^\mu \underline{u}_\nu + p_g \delta^\mu_\nu, \\ T^{\text{EM}\mu}_\nu &= b^2 \underline{u}^\mu \underline{u}_\nu + p_b \delta^\mu_\nu - \underline{b}^\mu \underline{b}_\nu, \\ T^\mu_\nu &= T^{\text{MA}\mu}_\nu + T^{\text{EM}\mu}_\nu. \end{aligned} \quad (5)$$

The MA term can be decomposed into a particle (PA) term: $T^{\text{PA}\mu}_\nu = \rho_0 \underline{u}_\nu \underline{u}^\mu$ and an enthalpy (EN) term. The MA term can be reduced to a free thermo-kinetic energy (MAKE) term, which

is composed of free particle (PAKE) and enthalpy (EN) terms:

$$\begin{aligned}
T^{\text{MAKE}\mu}_{\nu} &= T^{\text{MA}\mu}_{\nu} - \rho_0 \underline{u}^{\mu} \underline{\eta}_{\nu} / \alpha, \\
T^{\text{PAKE}\mu}_{\nu} &= (\underline{u}_{\nu} - \underline{\eta}_{\nu} / \alpha) \rho_0 \underline{u}^{\mu}, \\
T^{\text{EN}\mu}_{\nu} &= (e_g + p_g) \underline{u}^{\mu} \underline{u}_{\nu} + p_g \delta^{\mu}_{\nu},
\end{aligned} \tag{6}$$

such that $T^{\text{MAKE}\mu}_{\nu} = T^{\text{PAKE}\mu}_{\nu} + T^{\text{EN}\mu}_{\nu}$. Here, e_g is the internal energy density and $p_g = (\Gamma - 1)e_g$ is the ideal gas pressure with adiabatic index $\Gamma = 4/3$ ($\Gamma = 5/3$ may lead to somewhat different results ; (87, 88)). The sound speed is given as $c_s = \sqrt{\Gamma p_g / (\rho_0 + e_g + p_g)}$. The contravariant fluid-frame magnetic 4-field is given by \underline{b}^{μ} , which is related to the lab-frame 3-field via $\underline{b}^{\mu} = \underline{B}^{\nu} h^{\mu}_{\nu} / \underline{u}^{\mu}$ where $h^{\mu}_{\nu} = \underline{u}^{\mu} \underline{u}_{\nu} + \delta^{\mu}_{\nu}$ is a projection tensor that is the inverse metric on spatial hypersurfaces orthogonal to u^{μ} (giving an orthonormal comoving tetrad that is space-like diagonal) and that extracts the spatial part of the comoving magnetic field (giving $b^{\mu} u_{\mu} = 0$) and that in any basis gives $B^{\mu} = (-u^{\nu} B_{\nu}) u^{\mu} + h^{\mu}_{\nu} B^{\nu}$ so the field has been split into parts parallel and perpendicular to u^{μ} , and δ^{μ}_{ν} is the Kronecker delta function. The magnetic energy density (u_b) and pressure (p_b) are $u_b = p_b = \underline{b}^{\mu} \underline{b}_{\mu} / 2 = b^2 / 2$. The total pressure is $p_{\text{tot}} = p_g + p_b$, and plasma $\beta_{\text{plasma}} \equiv p_g / p_b$. The 4-velocity of a zero angular momentum observer (ZAMO) is $\underline{\eta}_{\mu} = \{-\alpha, 0, 0, 0\}$ where $\alpha = 1 / \sqrt{-g^{tt}}$ is the lapse, which is a convenient observer that follows worldlines with $\underline{dx}^i / dt = -\underline{\beta}^i$ with $\underline{\beta}^i = \alpha^2 g^{ti}$ such that $\underline{\eta}^{\mu} = (1/\alpha)\{1, -\underline{\beta}^i\}$. The BH metric can then be written as $ds^2 = -\alpha^2 dt^2 + h_{ij}(\underline{dx}^i + \underline{\beta}^i dt)(\underline{dx}^j + \underline{\beta}^j dt)$, which often simplifies calculations. We used this ZAMO to construct a frame that moves relative to the ZAMO with a time-like 4-velocity of $\underline{\tilde{u}}^{\mu} = \underline{u}^{\mu} - \gamma \underline{\eta}^{\mu}$ where $\gamma = -\underline{u}^{\alpha} \underline{\eta}_{\alpha}$. Spatial interpolations of this relative 4-velocity always lead to time-like 4-velocities (unlike interpolations of the lab-frame 3-velocity) and also give a unique time-like observer even inside the BH ergosphere (unlike the lab-frame 4-velocity that can have two time-like observers inside the ergosphere). So this relative 4-velocity is well-suited to numerical simulations that rely heavily upon spatial interpolations and must not lose

any information about the fluid frame in the ergosphere. For any 3-vector (e.g. \underline{B}^i), the “quasi-orthonormal” vector is $B_i \equiv \underline{B}^i \sqrt{g_{ii}}$ computed in spherical polar coordinates.

Magnetic flux conservation is given by the induction equation

$$\partial_t(\sqrt{-g}\underline{B}^i) = -\partial_j[\sqrt{-g}(\underline{B}^i\underline{v}^j - \underline{B}^j\underline{v}^i)], \quad (7)$$

where $g = \text{Det}(g_{\mu\nu})$ is the metric’s determinant, and the lab-frame 3-velocity is $\underline{v}^i = \underline{u}^i/\underline{u}^t$. No explicit viscosity or resistivity are included, but we used the energy conserving HARM scheme so all dissipation is captured (40, 89).

The energy-momentum conservation equations are only modified due to so-called numerical density floors that keep the numerical code stable as described in detail in the Appendix of (28). The injected densities were tracked and removed from all calculations.

1.4 Diagnostics

The discussion in this section follows that of (28). Diagnostics were computed from snapshots produced every $\sim 2r_g/c$. For quantities Q , averages over space ($\langle Q \rangle$) and time ($[Q]_t$) were performed directly on Q (e.g. on v_ϕ rather than on any intermediate values). Any flux ratio vs. time with numerator F_N and denominator F_D (F_D often being mass or magnetic flux) was computed as $R(t) = \langle F_N(t) \rangle / [\langle F_D \rangle]_t$. Time-averages were then computed as $[R]_t$.

1.4.1 Fluxes and Averages

For flux density F_d , the flux integral is

$$F(r) \equiv \int dA_{23} F_d, \quad (8)$$

where $dA_{23} = \sqrt{-g} d\underline{x}^{(2)} d\underline{x}^{(3)}$ ($dA_{\theta\phi}$ is the spherical polar version). For example, $F_d = \rho_0 \underline{u}^{(1)}$ gives $F = \dot{M}$, the rest-mass accretion rate. For weight w , the average of Q is

$$Q_w(r) \equiv \langle Q \rangle_w \equiv \frac{\int dA_{\theta\phi} w Q}{\int dA_{\theta\phi} w}, \quad (9)$$

All θ, ϕ angles are integrated over.

1.4.2 Disk Thickness Measurement

The disk's geometric half-angular thickness is given by

$$H/R \equiv \left(\left\langle (\theta - \theta_0)^2 \right\rangle_\rho \right)^{1/2}, \quad (10)$$

where we integrated over all θ for each r, ϕ , and $\theta_0 \equiv \pi/2 + \langle (\theta - \pi/2) \rangle_\rho$ was also integrated over all θ for each r, ϕ , and the final $H/R(r)$ was from ϕ -averaging with no additional weight or $\sqrt{-g}$ factor. This way of forming $H/R(r)$ works for slightly tilted thin disks or disordered thick disks. For a Gaussian distribution in density, this satisfies $\rho/(\rho[\theta = 0]) \sim \exp(-\theta^2/(2(H/R)^2))$.

The value of H/R is computed at various locations and times, while for this work we report the value at the initial pressure maximum in the untilted solutions and at $r \sim 30r_g$ in the evolved quasi-steady state solutions. The thickness at large distances from the BH does not change significantly as the flow evolves (28) or after tilt is introduced in the simulation. Note that, unlike expected from modern thick disk accretion theory, the BH jet compresses the disk causing the geometric H/R to drop as the disk approaches the BH (28).

1.4.3 Relative Tilt Measurement

The tilt of the disk rotation axis and jet direction with respect to the BH spin axis was measured using the angular momentum (86). The BH angular momentum vector is

$$J_{\text{BH}} = (aM \sin \theta_{\text{tilt},0} \hat{x}, 0, aM \cos \theta_{\text{tilt},0} \hat{z}), \quad (11)$$

with $\theta_{\text{tilt},0}$ is the initial tilt between the angular momentum vectors of the BH and the disk. The MHD angular momentum vector is

$$J_{\text{MHD}}(r) = \left[(J_{\text{MHD}})_x \hat{x}, (J_{\text{MHD}})_y \hat{y}, (J_{\text{MHD}})_z \hat{z} \right] \quad (12)$$

in an asymptotically flat space-time, where

$$(J_{\text{MHD}})_\rho = \frac{\epsilon_{\mu\nu\sigma\rho} L^{\mu\nu} \zeta^\sigma}{2} \quad (13)$$

for some frame with 4-velocity ζ^σ (for simplicity, we choose the Kerr-Schild lab-frame), and

$$L^{\mu\nu} = \int d\Sigma_\alpha (x^\mu T^{\nu\alpha} - x^\nu T^{\mu\alpha}), \quad (14)$$

where $d\Sigma_\alpha = \epsilon_{\beta\gamma\delta\alpha} dx^\beta dy^\gamma dz^\delta$ and the integral is performed for each radial shell. The unit vector \hat{y} points along the axis around which the BH is tilted and the unit vector \hat{z} points along the initial rotational axis of the disk.

The plasma's relative tilt angle is(19)

$$\theta_{\text{tilt}}(r) = \arccos \left[\frac{J_{\text{BH}} \cdot J_{\text{MHD}}(r)}{|J_{\text{BH}}| |J_{\text{MHD}}(r)|} \right]. \quad (15)$$

Just after the restart from a untilted simulation and instantly applying tilt, $\theta_{\text{tilt}}(r) \approx \theta_{\text{tilt},0}$ throughout the disk.

As in (28), the disk is defined with the spatial integral performed with weight $\rho_0 u^t$ (using ρ_0 alone gives similar results) and normalized by the weight's volume integral. The jet is defined by taking the integral only over the region with $b^2/\rho_0 \geq 1$ with no weight.

1.4.4 Efficiency of Energy Extraction Measurement

The rest-mass flux, specific energy flux, and specific angular momentum flux are respectively given by

$$\dot{M} = \left| \int \rho_0 \underline{u}^r dA_{\theta\phi} \right|, \quad (16)$$

$$e \equiv \frac{\dot{E}}{[\dot{M}]_t} = - \frac{\int T_t^r dA_{\theta\phi}}{[\dot{M}]_t}, \quad (17)$$

$$J \equiv \frac{\dot{J}}{[\dot{M}]_t} = \frac{\int T_\phi^r dA_{\theta\phi}}{[\dot{M}]_t}. \quad (18)$$

The net flow efficiency (efficiency of energy extraction from the BH) is given by

$$\eta = \frac{\dot{E} - \dot{M}}{[\dot{M}]_t} = \frac{\dot{E}^{\text{EM}}(r) + \dot{E}^{\text{MAKE}}(r)}{[\dot{M}_{\text{H}}]_t}. \quad (19)$$

Positive values correspond to an extraction of positive energy from the system at some radius. Values greater than 100% indicate that more energy goes out of the BH than goes in.

1.4.5 Inflow Equilibrium and Quasi-Steady State

Inflow equilibrium is defined as when the flow is in a complete quasi-steady-state and the accretion fluxes are constant (apart from noise) vs. radius and time. The inflow equilibrium timescale is

$$t_{\text{ie}} = N \int_{r_i}^{r_{\text{ie}}} dr \left(\frac{-1}{[\langle v_r \rangle_\rho]_t} \right), \quad (20)$$

for N inflow times from $r = r_{\text{ie}}$ and $r_i = 12r_g$ to focus on the more self-similar part of the flow far from the BH. The value of r_{ie} is measured directly from the simulation using Equation (20) rather than indirectly from an estimate of the α viscosity and disk scale-height. As in our prior work (28), we define the quasi-steady state out to some radius to mean that inflow equilibrium has been reached out to that radius under the condition that N is between 2 and 3.

1.4.6 Modes and Correlation Lengths

The flow structure was studied via the discrete Fourier transform of dq (related to quantity Q) along $x = r, \theta, \phi$ giving amplitude a_p for $p = n, l, m$, respectively. The averaged amplitude is

$$\langle |a_p| \rangle \equiv \langle |\mathcal{F}_p(dq)| \rangle \equiv \int_{\text{not } x} \left| \sum_{k=0}^{N-1} dq e^{\frac{-2\pi i p k}{N-1}} \right|, \quad (21)$$

computed at $r = r_{\text{H}}, 4r_g, 8r_g, 30r_g$. The x is one of r, θ, ϕ and “not x ” are others (e.g. θ, ϕ for $x = r$). The dq is (generally) a function of x on a uniform grid indexed by k of N cells that span: δr equal to $0.75r$ around r for $x = r$, π for $x = \theta$, and 2π for $x = \phi$. The N is chosen so

all structure from the original grid is resolved, while the span covered allows many modes to be resolved.

For all x , $dq \equiv \sqrt{-g} d\underline{x}^{(1)} d\underline{x}^{(2)} d\underline{x}^{(3)} \delta Q / q_N$. For $x = r, \theta$, we let $q_N = \int_{\text{not } x} \sqrt{-g} d\underline{x}^{(1)} d\underline{x}^{(2)} d\underline{x}^{(3)} \langle [Q]_t \rangle$, $\langle [Q]_t \rangle$ as the time- ϕ averaged Q , and $\delta Q = Q - \langle [Q]_t \rangle$. Using dq removes gradients with r, θ so the Fourier transform acts on something closer to periodic with constant amplitude (see also (90)). For $x = \phi$, we let $q_N = 1$ and $\delta Q = Q$ because the equations of motion are ϕ -ignorable. For $x = \theta, \phi$, the radial integral is computed within $\pm 0.1r$. For $x = r, \theta$, the ϕ integral is over all 2π . For $x = r, \phi$, the θ integral is over all π . For all x cases, the θ range of values is over either the disk or jet (as defined earlier), where these regions are defined via ϕ -averaged quantities at each time. Notice we averaged the mode's absolute amplitude, because the amplitude of $\langle \delta Q \rangle$ de-resolves power (e.g. $m = 1$ out of phase at different θ gives $\langle \delta Q \rangle \rightarrow 0$ and $a_m \rightarrow 0$) and is found to underestimate small-scale structure.

We also computed the correlation length: $\lambda_{x,\text{cor}} = x_{\text{cor}} - x_0$, where $x_0 = 0$ for $x = \theta, \phi$ and x_0 is the inner radius of the above given radial span for $x = r$, where $n_{\text{cor}} = \delta r / \lambda_{r,\text{cor}}$, $l_{\text{cor}} = \pi / \lambda_{\theta,\text{cor}}$, and $m_{\text{cor}} = (2\pi) / \lambda_{\phi,\text{cor}}$. The Wiener-Khinchin theorem for the auto-correlation gives

$$\exp(-1) = \frac{\mathcal{F}_{x=x_{\text{cor}}}^{-1} [\langle |a_{p>0}| \rangle^2]}{\mathcal{F}_{x=x_0}^{-1} [\langle |a_{p>0}| \rangle^2]}, \quad (22)$$

where $\mathcal{F}^{-1}[\langle |a_{p>0}| \rangle^2]$ is the inverse discrete Fourier transform of $\langle |a_p| \rangle^2$ but with $\langle a_0 \rangle$ reset to 0 (i.e. mean value is excluded).

Turbulence (or flow structure in general) is resolved for grid cells per correlation length,

$$Q_{p,\text{cor}} \equiv \frac{\lambda_{x,\text{cor}}}{\Delta_x}, \quad (23)$$

of $Q_{p,\text{cor}} \geq 6$, for $x = r, \theta, \phi$ and $p = n, l, m$, respectively. Otherwise, modes are numerically damped on a dynamical timescale (even $Q = 5$ would not indicate the mode is marginally resolved, because numerical noise can keep $Q \approx 5$ at increasing resolution until finally the mode is actually resolved – finally leading to an increasing $Q \geq 6$ with increasing resolution

; as seen by (91)). Reported $Q_{p,\text{cor}}$ take $1/\Delta_x$ as the number of grid cells covering the span of $\lambda_{x,\text{cor}}$ as centered on: middle of $x^{(1)}$ within the used radial span for $x = r$, $\theta \sim \pi/2$ (a reasonable approximation even for tilted models when this is measured at $r \approx 8r_g$) for $x = \theta$ for the disk and $\theta \sim 0$ for $x = \theta$ for the jet, and anywhere for $x = \phi$.

1.4.7 The Magneto-Rotational Instability

The MRI is a linear instability with fastest growing wavelength of

$$\lambda_{x,\text{MRI}} \approx 2\pi \frac{|v_{x,A}|}{|\Omega_{\text{rot}}|}, \quad (24)$$

for $x = \theta, \phi$, where $|v_{x,A}| = \sqrt{b_x b^x / \epsilon}$ is the x -directed Alfvén speed, $\epsilon \equiv b^2 + \rho_0 + e_g + p_g$, and $r\Omega_{\text{rot}} = v_{\text{rot}}$. λ_{MRI} is accurate for $\Omega_{\text{rot}} \propto r^{-5/2}$ to r^{-1} . Ω_{rot}, v_A were separately angle-volume-averaged at each r, t .

The MRI is resolved for grid cells per wavelength in the $x = \theta, \phi$ directions,

$$Q_{x,\text{MRI}} \equiv \frac{\lambda_{x,\text{MRI}}}{\Delta_x}, \quad (25)$$

of $Q_\theta \gtrsim 10$ and $Q_\phi \gtrsim 20$ (92), where $\Delta_r \approx d\underline{x}^{(1)}(dr/d\underline{x}^{(1)})$, $\Delta_\theta \approx rd\underline{x}^{(2)}(d\theta/d\underline{x}^{(2)})$, and $\Delta_\phi \approx r \sin \theta d\underline{x}^{(3)}(d\phi/d\underline{x}^{(3)})$. Volume-averaging was applied to $v_{x,A}/\Delta_x$ and $|\Omega_{\text{rot}}|$ were separately θ, ϕ -volume-averaged before forming $Q_{x,\text{MRI}}$.

The MRI suppression factor corresponds to the number of MRI wavelengths across the full disk:

$$S_{d,\text{MRI}} \equiv \frac{2r(H/R)}{\lambda_{\theta,\text{MRI}}}. \quad (26)$$

Wavelengths $\lambda < 0.5\lambda_{\theta,\text{MRI}}$ are stable, so the linear MRI is suppressed for $S_{d,\text{MRI}} < 1/2$ when no unstable wavelengths fit within the full disk (93, 94). $S_{d,\text{MRI}}$ (or $S_{d,\text{weak,MRI}}$) uses averaging weight $w = (b^2\rho)^{1/2}$ (or $w = \rho$), condition $\beta_{\text{plasma}} > 1$, and excludes regions where density floors are activated. Weight $w = (b^2\rho)^{1/2}$ is preferred, because much mass flows in current

sheets where the magnetic field vanishes and yet the MRI is irrelevant. When computing the averaged $S_{d,\text{MRI}}$, v_A and $|\Omega_{\text{rot}}|$ were separately θ, ϕ -volume-averaged within $\pm 0.2r$ for each t, r . The averaged $S_{d,\text{MRI}}$ is at most 30% smaller than $S_{d,\text{weak,MRI}}$.

A measure of the magnetic stress per unit pressure given by

$$\alpha_{\text{mag}} \approx -\frac{b_r(b_\phi \sqrt{g^{\phi\phi}})}{p_b}, \quad (27)$$

can be used to determine how well-converged a numerical solution might be for MRI-dominated disk simulations. A value of $\alpha_{\text{mag}} \geq 0.4$ indicates a well-converged MRI-dominated simulation (92, 95). The numerator and denominator are separately volume averaged in θ, ϕ for each r . Note that $\sin(2\theta_b) = \alpha_{\text{mag}}$ for tilt angle θ_b (95). This measure is weakly applicable for our solutions where the MRI is suppressed and strong effects occur due to BH spin. However, at least for our thinner disk models this measure seems to roughly be applicable. For our thick disk models, the large amount of trapped magnetic flux and high BH spins lead to this measuring more about the angular momentum transported out from the BH into the disk than the MRI within the disk. For such thick disks, retrograde spins lead to negative α_{mag} (28).

1.5 Physical and Numerical Models

This section describes our models. The model names are in the form AxByNzTp, where x is the approximate value of the BH spin, y identifies the field geometry (p=poloidal, f=flipping poloidal, t=toroidal), z identifies the normalization of the magnetic field, and p identifies the tilt (tilt is zero if not given). This is the same type of notation we have used previously(28), where for this paper only poloidal or poloidal flipping models are considered. For instance, our model A0.94BfN40T0.3 had a spinning BH ($j = 0.9375$), a poloidal field that flips polarity with radius, $\beta_{\text{plasma,min}} \approx 40$ (i.e. smallest value of plasma β_{plasma} is 40), and a tilt of 0.3 radians.

All tilted models are continuations of the models without tilt given elsewhere(28)with parameters given in their tables 1 and 2. The relative tilt was imposed (via a change in the BH spin

axis) at a time $t = 8000r_g/c$ for thick disk models, $t = 10000r_g/c$ for thinner disk models except for the $a = 0.99$ models that used $t = 15000r_g/c$. The thick disk models ran from $8000r_g/c$ to roughly $17000r_g/c$, after which the initial magnetic field polarity inversion reaches the black hole, so no measurements are reported after this time. The thinner disk models with $|j| = 0.9$ ran from $10000r_g/c$ to roughly $22000r_g/c$, and the thinner disk models with $j = 0.99$ ran from $15000r_g/c$ to roughly $27000r_g/c$. These thinner disk models have no polarity inversions in the initial conditions. These durations allow the disk and jet to reach a quasi-steady state out to about $r \sim 40r_g$ within which results are reported.

1.5.1 Physical Models

The details of the original simulation’s initial mass distribution (an isentropic hydro-equilibrium torus), magnetic field distribution (poloidal magnetic field loops), and velocity are as provided in (28). We only studied magnetic field configurations that led to a saturated magnetic field strength value near the BH, and we only studied cases that generate sufficiently large-scale magnetic field to produce a jet (85, 96).

Our models were designed so that near the horizon the poloidal ($R-z$) magnetic flux reached a saturation point independent of the initial poloidal magnetic flux (4,34,28), which allowed us to provide robust results that are insensitive to any larger amount of magnetic flux available in the surrounding medium (97). In this sense, we identify the magnetic field strength reached as “natural” because it would require fine-tuning or an uncommon accident for the magnetic flux supply to be near saturation but somehow not simply far below or far beyond that required for near-BH saturation. A supply far below saturation would not lead to powerful jets as required by observations for many systems, while a large supply would simply lead to saturation out to some arbitrarily large distance and so not affect the near-BH dynamics.

Our initial magnetic flux supply was still finite, and our $H/R \sim 0.3$ models did not (and

would not) reach a fully saturated state beyond $r \sim 30r_g$ (34), while our $H/R \sim 0.6$ models have enough magnetic flux supply to reach magnetic flux saturation out to $r \sim 100r_g$ (28).

Our general relativistic magnetized disk simulations started with a tilted BH whose spin originally pointed towards the vertical (z) direction (28), and then (for this work) that BH spin direction was suddenly rotated by an angle $\theta_{\text{tilt},0}$ around another perpendicular axis (y -axis for definiteness) leading to the spin axis pointing more towards the x -axis for larger $\theta_{\text{tilt},0}$. A value of $\theta_{\text{tilt},0} = 0$ means no tilt, while $\theta_{\text{tilt},0} = 90^\circ$ means maximal tilt, while $\theta_{\text{tilt},0} = 180^\circ$ means the BH was rotated so much that the spin value of j is simply the opposite sign. Hence, by symmetry we only need to consider $\theta_{\text{tilt},0} = 0^\circ$ to 90° for dimensionless spins in the range $-1 \leq j \leq 1$.

For thick disks with height (H) to radius (R) ratio of $H/R \approx 0.6 \approx 34^\circ$ (the evolved quasi-steady state value of H/R at $r \sim 30r_g$, where $H/R \approx 0.6$ at the initial torus pressure maximum at $r = 100r_g$), we obtained quasi-steady solutions with tilts $\theta_{\text{tilt},0} = 0^\circ, 20^\circ, 40^\circ, 90^\circ$ with spin $j = +0.9375$. Note that $j = -0.9375$ is expected to behave similarly to a model with $j = +0.9375$ because these thick disk models result in the entire disk being forced to rotate in the same direction as the BH spin – giving a result that is completely independent of the initial disk angular momentum out to $r \sim 40r_g$ (28).

For thinner disks with $H/R \approx 0.3 \approx 17^\circ$ (the evolved quasi-steady state value of H/R at $r \sim 30r_g$, where $H/R \approx 0.2$ at the initial torus pressure maximum at $r \sim 35r_g$), we obtained quasi-steady solutions with tilts $\theta_{\text{tilt},0} = 0^\circ, 9^\circ, 17^\circ, 34^\circ, 90^\circ$ with spins $j = -0.9, +0.9, +0.99$.

Note that j is really a proxy for the actual BH angular frequency given by $\Omega_H = jc/2r_H$ (maximum value of 0.5) that sets the rate of frame-dragging. A value of $j = 0.5, 0.9, 0.9375, 0.99, 1$ gives $\Omega_H \approx 0.13, 0.31, 0.35, 0.43, 0.5$. Hence, a value of $j = 0.9$ is really a middle-range value for the BH rotation rate. For small values of $j \lesssim 0.5$ that operate at less than a fifth of the maximum rotation rate, the effects of frame-dragging or tilt are expected to be none to minimal. Of course, in the limit of $j = 0$ then the BH space-time is spherical and there is no physical

manifestation of any chosen $\theta_{\text{tilt},0}$.

Table S1 gives a list of diagnostics that we have measured as discussed in section 1.4. These diagnostics are measured just like in our prior work on untilted simulations (28). A list of identical diagnostic measurements for other untilted simulations (including those used as a starting point for the tilted simulations) can be found in extensive tables elsewhere (28). The table shows that Υ and η remain relatively high for all tilted models, with some drop seen for fully tilted models.

1.5.2 Numerical Models

The resolution is chosen equal or higher than required to resolve turbulence and physical disk instabilities, as discussed previously (28). We chose a resolution $N_r \times N_\theta \times N_\phi$ that had a grid aspect ratio of 1:1:1 for most of the domain for $r \lesssim 40r_g$. The grid is fully 3D with a ϕ -range of 2π . This allowed the ϕ dimension to be treated equally to the $r - \theta$ dimensions. Thick disk models used a resolution of $N_r \times N_\theta \times N_\phi = 272 \times 128 \times 256$, while thinner disk models used $N_r \times N_\theta \times N_\phi = 288 \times 128 \times 128$ (twice larger N_ϕ than our prior models for $|j| = 0.9$).

In our prior work on otherwise identical untilted simulations (28), we used numerous diagnostics and numerical convergence quality measures to check that structures in the disk and jet were properly resolved (our measures are extensions of those discussed elsewhere (90–92, 95, 98)). In our prior study, for our thick disk models, we found that $272 \times 128 \times 256$ was sufficient to overly resolve the MRI, well resolve the radial and azimuthal correlation lengths that describe the characteristic sizes of structures in the disk and jet, and marginally resolve the vertical correlation length due to magnetic Rayleigh-Taylor modes that lead to disk compression. All thinner disk models were similarly resolved, except the $|j| = 0.9$ models that used $N_\phi = 64$ did slightly under-resolve the azimuthal correlation length by a factor less than two. In convergence studies in that paper, the number of grid cells per azimuthal correlation length was

seen to scale with resolution as expected, so in this paper we doubled the N_ϕ resolution (from $N_\phi = 64$ to $N_\phi = 128$) to ensure that untilted thinner disk $|j| = 0.9$ simulations would properly resolve all correlation lengths.

For these new tilted simulations, as in our prior work (28), we confirmed that the MRI and turbulence were resolved both initially and at late times through-out the disk and jet at many different radii. Table S2 gives a list of convergence quality measures as computed in section 1.4. These measures were computed the same way as in our prior work (28). A list of identical convergence quality measurements for the untilted simulations (used as a starting point for the tilted simulations) can be found in extensive tables elsewhere (28). Since the tilted simulations just continue the untilted simulations, the initial MRI convergence quality measures were the same as already reported elsewhere (28). In all the untilted models that we used for the tilted simulations, the initial MRI was well-resolved.

In all cases, the convergence quality measures indicated that the simulations are at least marginally converged and some aspects were well-converged, which is expected given that was how we chose the resolutions as based upon similar measures for otherwise identical untilted simulations.

As in our prior work (28), we also explicitly checked convergence of all our measures, including for disk tilt and jet tilt at late times, by repeating our thinner disk $j = 0.99$ $\theta_{\text{tilt}} = 1.5708$ simulations with a resolution of $144 \times 64 \times 32$ and $144 \times 64 \times 64$. We did not double the resolution to $576 \times 256 \times 256$ because such a single model would use about 16 million central processing unit (CPU)-hours on Kraken. Further, as we see next, convergence was already been obtained for Υ and θ_{tilt} that we are focused on.

As found in our prior work for untilted models, the value of Υ that controls the jet magnetic flux was insensitive to such changes in resolution. The disk and jet align with $\theta_{\text{rot}} \approx 0.1$ at $r \approx 4r_g$ and $\theta_{\text{rot}} \approx 0.6$ at $r \approx 30r_g$ as with the higher resolution model. The jet magnetic flux is

what leads to the EM force that aligns the disk with the BH, so the “magneto-spin alignment” effect is not sensitive to such changes in resolution. This is expected because the amount of trapped magnetic flux is set primarily by non-turbulent force balance against the large-scale magnetic field, and the EM jet power (and so force) does not strongly depend upon resolving the small-scale turbulence in the disk.

The entire set of new tilted simulations (as continuations of untilted simulations) required about 22 million CPU-hours on the Extreme Science and Engineering Discovery Environment (XSEDE) Kraken cluster and another 11 million CPU-hours on the NAS Pleiades Westmere cluster.

Table S1: Simulation Physical Setup and Results

ModelName	j	$\theta_{\text{tilt},0}$	T_f	$T_i^a - T_f^a$	r_{in}	r_{out}	H/R	\dot{M}_{H}	Υ_{H}	η_{H}
A0.94BfN40	0.9375	0	26548	8000–17000	12	29	0.6	48	17	240
A0.94BfN40T0.35	0.9375	0.35	20376	14000–17000	12	30	0.59	42	17	250
A0.94BfN40T0.7	0.9375	0.7	18656	14000–17000	12	30	0.59	67	12	67
A0.94BfN40T1.5708	0.9375	1.5708	18132	14000–17000	12	30	0.68	43	12	73
A-0.9N100	-0.9	0	20060	11000–20060	12	30	0.31	18	6.6	32
A-0.9N100T0.15	-0.9	0.15	23280	17000–23280	12	30	0.35	21	5.4	18
A-0.9N100T0.3	-0.9	0.3	22095	17000–22095	12	30	0.36	23	4.5	10
A-0.9N100T0.6	-0.9	0.6	20400	17000–20400	12	30	0.35	22	3.7	7
A-0.9N100T1.5708	-0.9	1.5708	23580	17000–23580	12	30	0.37	22	4.2	11
A0.9N100	0.9	0	19895	11000–19895	12	30	0.31	11	10	100
A0.9N100T0.15	0.9	0.15	20290	17000–20290	12	30	0.32	6.1	12	150
A0.9N100T0.3	0.9	0.3	22585	17000–22585	12	30	0.35	14	8.8	69
A0.9N100T0.6	0.9	0.6	21010	17000–21010	12	30	0.34	14	8.9	70
A0.9N100T1.5708	0.9	1.5708	24385	17000–21000	12	30	0.41	22	4.8	16
A0.99N100	0.99	0	31400	15000–31400	12	30	0.33	9.8	9.1	130
A0.99N100T0.15	0.99	0.15	25120	22000–25120	12	30	0.36	11	9	130
A0.99N100T0.3	0.99	0.3	25085	22000–25085	12	30	0.36	9.3	8.1	110
A0.99N100T0.6	0.99	0.6	25965	22000–25965	12	30	0.38	7.8	9.3	140
A0.99N100T1.5708	0.99	1.5708	28690	22000–28690	12	30	0.55	11	5.2	34

Table S1: The columns correspond to (1) the model name, (2) BH spin, (3) initial tilt, (4) final time of the simulation, (5) time-averaging range for any time-averaged quantity, (6) inner radius used to measure some quantities (Q_{x,MRI_i} , S_{d,MRI_i} in Table S2), (7) outer radius used to measure some quantities (Q_{x,MRI_o} , S_{d,MRI_o} in Table S2), (8) accurate disk thickness at $r \approx 30r_g$, (9) mass accretion rate, (10) dimensionless magnetic flux on the horizon, and (11) BH efficiency.

Movie S1

This movie shows inner distances for the evolved state of the model with $j = 0.99$, $\theta_{\text{tilt},0} = 1.5708$, and $H/R \sim 0.3$ as shown in Figs. 1-2 in the report (See also <http://youtu.be/XxIzazsEsg>, 20MB mp4 for full 1080p HD). The movie shows the full 3D structure that is difficult to see in a single 2D image because the BH, jet, and disk have axes that do not sit in the same two-dimensional plane. The movie shows the same rendering as Fig. 1 (without the vector field surface and with density volume rendering replaced by density isosurface) with the view rotated around a single axis so one can clearly see the full 3D structure of the BH spin direction, disk

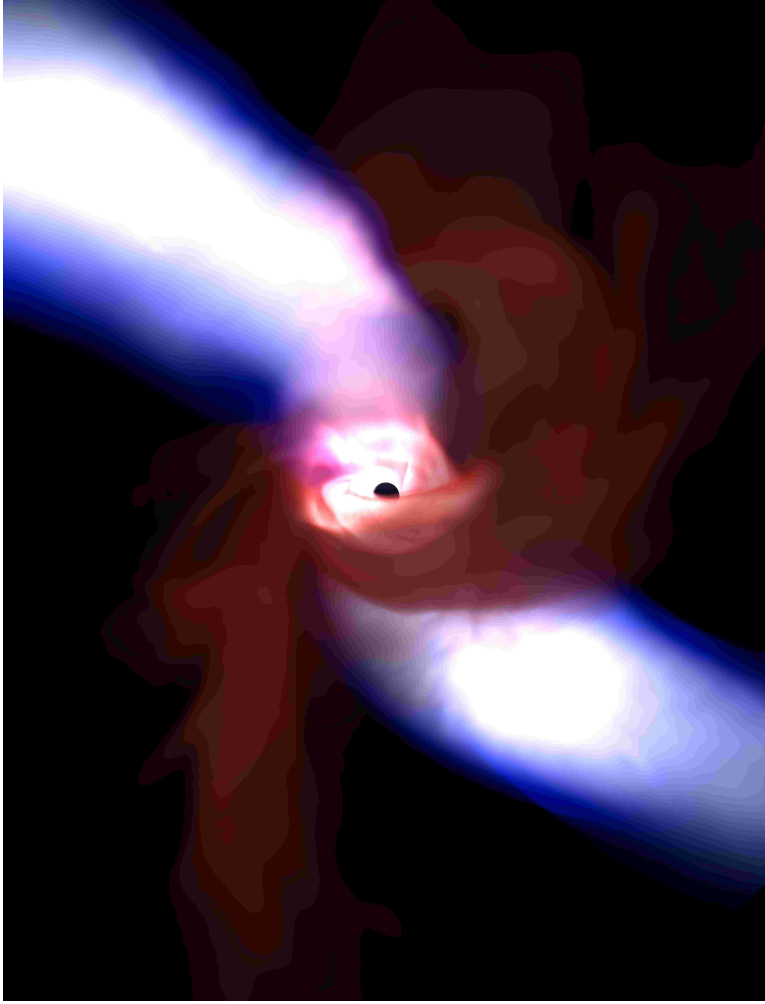


Figure S1: Artistic 3D rendering showing an evolved 3D snapshot, similar to Fig. 1 in the report, for a model with $j = 0.99$, initial relative tilt $\theta_{\text{tilt},0} \approx 90^\circ$, and disk thickness of $H/R \sim 0.3$. The rotating BH is shown as a black sphere and sits at the center of the box of size of about $r = -40r_g$ to $r = +40r_g$ in the vertical dimension and otherwise about $r = -30r_g$ to $r = +30r_g$ in the other dimensions. The jet is shown by the region where the magnetic energy density per unit rest-mass energy density is greater than about 10 up to about 100 (blue-white volume rendering). The logarithm of the density in the disk region is shown close to the BH (red-white volume rendering). The BH spin axis points vertically. Near the BH, the disk rotational axis and jet direction are strongly aligned with the BH spin axis. However, at $t = 0$ and at large radius for all evolved times, the disk and jet axes pointed completely horizontally, i.e. perpendicular to the vertical axis. This shows the strong magnetic torques have caused the disk and jet to change orientation by 90° and to become aligned with the BH spin axis near the BH. At larger distances, the jet gradually bends away from the BH spin axis and aligns with the disk rotational axis at large distances. This leads to the jet and counter-jet being offset at large distances.

Table S2: Simulation Convergence Study

ModelName	α_{mag}	$Q_{n,\text{cor}},$ $\{\rho_0, b^2\}$	$Q_{l,\text{cor}},$ $\{\rho_0, b^2\}$	$Q_{m,\text{cor}},$ $\{\rho_0, b^2\}$	$Q_{\theta,\text{MRI}}$ $\{i, o\}$	$Q_{\phi,\text{MRI}}$ $\{i, o\}$	$S_{\text{d,MRI}}$ $\{i, o\}$
A0.94BfN40	0.26	22, 21	6, 12	19, 18	110, 120	380, 540	0.33, 0.34
A0.94BfN40T0.35	0.22	26, 25	10, 14	36, 35	110, 120	460, 710	0.33, 0.34
A0.94BfN40T0.7	0.35	27, 27	18, 20	31, 32	160, 130	440, 550	0.24, 0.35
A0.94BfN40T1.5708	0.32	25, 27	14, 17	23, 21	140, 130	330, 610	0.24, 0.33
A-0.9N100	0.49	23, 22	9, 11	10, 10	110, 35	44, 42	0.29, 0.84
A-0.9N100T0.15	0.51	20, 21	10, 15	8, 10	100, 77	42, 54	0.4, 0.42
A-0.9N100T0.3	0.52	22, 21	15, 20	9, 13	70, 71	39, 54	0.55, 0.48
A-0.9N100T0.6	0.47	22, 22	16, 20	9, 9	99, 62	54, 57	0.39, 0.55
A-0.9N100T1.5708	0.45	22, 22	24, 28	11, 14	97, 83	51, 74	0.41, 0.43
A0.9N100	0.54	29, 28	8, 10	8, 8	120, 42	60, 44	0.27, 0.79
A0.9N100T0.15	0.48	27, 26	9, 13	8, 8	160, 56	69, 50	0.24, 0.59
A0.9N100T0.3	0.53	27, 27	12, 17	8, 13	100, 69	62, 56	0.38, 0.46
A0.9N100T0.6	0.49	27, 28	17, 21	8, 15	87, 60	55, 48	0.41, 0.56
A0.9N100T1.5708	0.38	30, 29	24, 28	9, 12	100, 68	79, 54	0.45, 0.55
A0.99N100	0.53	22, 20	6, 8	7, 7	110, 67	66, 54	0.33, 0.56
A0.99N100T0.15	0.5	22, 20	6, 7	7, 8	93, 87	61, 59	0.41, 0.41
A0.99N100T0.3	0.5	22, 20	7, 7	7, 8	130, 80	72, 55	0.3, 0.47
A0.99N100T0.6	0.46	20, 20	6, 7	8, 10	75, 53	65, 58	0.49, 0.64
A0.99N100T1.5708	0.24	22, 23	11, 11	12, 13	100, 120	86, 96	0.42, 0.35

Table S2: The columns correspond to (1) the model name, (2) α_{mag} with radial averaging over $r = 12r_g$ to $r = 20r_g$, (3) number of grid cells per correlation length in the radial (n) direction, (4) number of grid cells per correlation length in the vertical-angular (l) direction, (5) number of grid cells per correlation length in the azimuthal (m) direction (all correlation lengths are measured for the rest-mass density and magnetic energy density at $r \approx 8r_g$, where beyond the horizon all values are similar), (6) number of grid cells per vertical-angular MRI wavelength, (7) number of grid cells per azimuthal MRI wavelength, and (8) MRI suppression factor. The inner (i) and outer (o) radius values for columns 6,7,8 are measured at the inner and outer radii given in Table S1.

plane near the BH, jet direction, and disk rotational axis at larger distances (as represented by the orange cylinder).

Movie S2

This movie shows the outer distances for the evolved state of the model with $j = 0.99$, $\theta_{\text{tilt},0} = 1.5708$, and $H/R \sim 0.3$ as shown in Figs. 1-2 in the report (See also <http://youtu.be/25WGtFVcHe0>, 11MB mp4 for full 1080p HD). The movie shows the same rendering as Fig. 2 with the view rotated around a single axis so one can clearly see the full 3D structure of the jet near the BH, the disk plane near the BH, the jet direction as it deviates at larger radii, the disk material that is pushed back into a warp by the jet, and the disk rotational axis at larger distances (as seen in the outer disk isosurface and represented by the orange cylinder).

References and Notes

40. C. F. Gammie, J. C. McKinney, G. Tóth, *ApJ* **589**, 444 (2003).
41. S. C. Noble, C. F. Gammie, J. C. McKinney, L. Del Zanna, *ApJ* **641**, 626 (2006).
42. A. Tchekhovskoy, J. C. McKinney, R. Narayan, *MNRAS* **379**, 469 (2007).
43. C. Gammie, F., J. C. McKinney, G. Tóth, *Astrophysics Source Code Library:1209.005* (2012).
44. M. J. Rees, *Nature* **211**, 468 (1966).
45. M. J. Rees, *Nature* **219**, 127 (1968).
46. R. D. Blandford, C. F. McKee, M. J. Rees, *Nature* **267**, 211 (1977).
47. A. C. Fabian, M. J. Rees, W. R. Stoeger, D. Maccagni, *Nature* **260**, 683 (1976).
48. M. J. Rees, *Nature* **275**, 516 (1978).
49. M. J. Rees, M. C. Begelman, R. D. Blandford, E. S. Phinney, *Nature* **295**, 17 (1982).
50. R.-S. Lu, *et al.*, *ApJ* **757**, L14 (2012).
51. W. H. Press, *ApJ* **175**, 243 (1972).
52. M. D. Pollock, *Royal Society of London Proceedings Series A* **350**, 239 (1976).
53. M. D. Pollock, W. P. Brinkmann, *Royal Society of London Proceedings Series A* **356**, 351 (1977).
54. J. Bicak, V. Janis, *MNRAS* **212**, 899 (1985).
55. A. N. Aliev, D. V. Gal'tsov, *Soviet Physics Uspekhi* **32**, 75 (1989).

56. A. N. Aliev, D. V. Galt'sov, *Ap&SS* **135**, 81 (1987).
57. R. D. Blandford, *Science* **295**, 1653 (2002).
58. R. Narayan, E. Quataert, *Science* **307**, 77 (2005).
59. J.-P. De Villiers, J. F. Hawley, *ApJ* **577**, 866 (2002).
60. C. F. Gammie, S. L. Shapiro, J. C. McKinney, *ApJ* **602**, 312 (2004).
61. P. C. Fragile, *ApJ* **706**, L246 (2009).
62. P. C. Fragile, O. M. Blaes, *ApJ* **687**, 757 (2008).
63. J. Dexter, P. C. Fragile, *ApJ* **730**, 36 (2011).
64. J. Dexter, P. C. Fragile, *ArXiv/1204.4454* (2012).
65. Z. B. Etienne, V. Paschalidis, S. L. Shapiro, *ArXiv/1209.1632* (2012).
66. P. Natarajan, J. E. Pringle, *ApJ* **506**, L97 (1998).
67. A. L. Kinney, *et al.*, *ApJ* **537**, 152 (2000).
68. P. C. Fragile, G. J. Mathews, J. R. Wilson, *ApJ* **553**, 955 (2001).
69. J. Dennett-Thorpe, *et al.*, *MNRAS* **330**, 609 (2002).
70. T. J. Maccarone, *MNRAS* **336**, 1371 (2002).
71. A. R. King, S. H. Lubow, G. I. Ogilvie, J. E. Pringle, *MNRAS* **363**, 49 (2005).
72. A. Caproni, Z. Abraham, H. J. Mosquera Cuesta, *ApJ* **638**, 120 (2006).
73. A. Caproni, M. Livio, Z. Abraham, H. J. Mosquera Cuesta, *ApJ* **653**, 112 (2006).

74. A. Caproni, Z. Abraham, M. Livio, H. J. Mosquera Cuesta, *MNRAS* **379**, 135 (2007).
75. M. Volonteri, M. Sikora, J.-P. Lasota, *ApJ* **667**, 704 (2007).
76. R. G. Martin, R. C. Reis, J. E. Pringle, *MNRAS* **391**, L15 (2008).
77. E. J. Hodges-Kluck, C. S. Reynolds, M. C. Miller, C. C. Cheung, *ApJ* **717**, L37 (2010).
78. T. Fragos, M. Tremmel, E. Rantsiou, K. Belczynski, *ApJ* **719**, L79 (2010).
79. D. Falceta-Gonçalves, A. Caproni, Z. Abraham, D. M. Teixeira, E. M. de Gouveia Dal Pino, *ApJ* **713**, L74 (2010).
80. A. K. Kulkarni, *et al.*, *MNRAS* **414**, 1183 (2011).
81. W.-H. Lei, B. Zhang, H. Gao, *ArXiv/1202.4231* (2012).
82. M. Mościbrodzka, C. F. Gammie, J. C. Dolence, H. Shiokawa, P. K. Leung, *ApJ* **706**, 497 (2009).
83. R. V. Shcherbakov, R. F. Penna, J. C. McKinney, *ApJ* **755**, 133 (2012).
84. A. E. Broderick, V. L. Fish, S. S. Doeleman, A. Loeb, *ApJ* **735**, 110 (2011).
85. J. C. McKinney, R. D. Blandford, *MNRAS* **394**, L126 (2009).
86. P. C. Fragile, P. Anninos, *ApJ* **623**, 347 (2005).
87. J. C. McKinney, C. F. Gammie, *ApJ* **611**, 977 (2004).
88. A. Mignone, J. C. McKinney, *MNRAS* **378**, 1118 (2007).
89. J. C. McKinney, *MNRAS* **367**, 1797 (2006).
90. K. Beckwith, P. J. Armitage, J. B. Simon, *MNRAS* **416**, 361 (2011).

91. H. Shiokawa, J. C. Dolence, C. F. Gammie, S. C. Noble, *ApJ* **744**, 187 (2012).
92. J. F. Hawley, X. Guan, J. H. Krolik, *ApJ* **738**, 84 (2011).
93. S. A. Balbus, J. F. Hawley, *Rev. Mod. Phys.* **70**, 1 (1998).
94. M. E. Pessah, D. Psaltis, *ApJ* **628**, 879 (2005).
95. K. A. Sorathia, C. S. Reynolds, J. M. Stone, K. Beckwith, *ApJ* **749**, 189 (2012).
96. K. Beckwith, J. F. Hawley, J. H. Krolik, *ApJ* **678**, 1180 (2008).
97. R. Narayan, I. V. Igumenshchev, M. A. Abramowicz, *PASJ* **55**, L69 (2003).
98. X. Guan, C. F. Gammie, J. B. Simon, B. M. Johnson, *ApJ* **694**, 1010 (2009).